Photoelectrochemical properties and photodegradation of organic pollutants using hematite hybrids modified by gold nanoparticles and graphitic carbon nitride

Rajendra C. Pawar [a], Youngjun Pyo [a], Sung Hoon Ahn [b], Caroline Sunyong Lee [a,*]

[a] Department of Materials Engineering, Hanyang University, Ansan 426-791, Gyeonggi-do, South Korea
[b] School of Mechanical & Aerospace Engineering, Seoul National University, Seoul 151-742, South Korea

ARTICLE INFO

ABSTRACT

In this study, heterojunctions of gold (Au) nanoparticles with three different average sizes (26, 20, and 12 nm in diameter), graphitic carbon nitride (g-C_3N_4) sheets, and rhombohedral hematite (Fe_2O_3) hybrid photocatalysts were fabricated via sonication at room temperature and used in the degradation of rhodamine B (RhB) dye under visible irradiation. The Au sensitized g-C_3N_4/Fe_2O_3 hybrid photocatalyst using 12 nm-sized Au particles, exhibited apparent rate constant of 31.6×10^{-3} min^{-1}, nearly 19-fold higher than that of pure hematite ($Fe_2O_3 = 1.7 \times 10^{-3}$ min^{-1}), and higher than those of the other hybrid samples. The superior performance of the Au/g-C_3N_4/Fe_2O_3 hybrid was attributed to a potential energy level difference, high optical absorbance, and the effective separation of photogenerated charge carriers. Additionally, the Au sensitized g-C_3N_4/Fe_2O_3 hybrid using 12 nm-sized Au particles, showed the highest specific surface area (46.5 m^2 g^{-1}), compared with that of pure Fe_2O_3 (5.5 m^2 g^{-1}) and g-C_3N_4/Fe_2O_3 (29.7 m^2 g^{-1}) hybrid photocatalysts, showing numerous available sites for dye adsorption and degradation. Moreover, the transient photoresponse and open-circuit voltage decay clearly showed a high photocurrent and longer charge carrier lifetime, respectively. Reusability tests confirmed that the Au/g-C_3N_4/Fe_2O_3 hybrid photocatalyst was highly stable and recyclable. Hence, the work presented demonstrates the efficient, stable Au/g-C_3N_4/Fe_2O_3 hybrid photocatalyst for degradation of toxic pollutants under visible irradiation.

© 2015 Elsevier B.V. All rights reserved.

1. Introduction

Semiconductor nanostructure-based photoelectrochemical (PEC) water splitting and purification are one of the most prominent technologies in the direct use of solar energy for the production of hydrogen and photodegradation of a wide range of organic pollutants [1,2], and are potentially the best of the key green technologies in terms of a replacement for conventional energy resources [3]. Since the water-splitting demonstration by Fujishima and Honda, an enormous amount of work has been performed on water splitting and pollutant degradation using solar light [4–7]. Most reports have focused on developing efficient, cost-effective, and environmentally benign photocatalysts using various organic/inorganic semiconductors and a simple fabrication process. However, to achieve the desired efficiency, the designed photocatalysts should have a better light response, minimal recombination of photogenerated charge carriers, a high stability, and should utilize almost the entire spectrum of sunlight [8,9]. Interestingly, various semiconductor heterojunctions have been fabricated, including metal oxides (TiO_2, ZnO, and WO_3), chalcogenides (CdSe, CdS, and CdTe), metal nanoparticles, and polymers (polyaniline and polypyrrole) to achieve better photocatalytic activity and stability [10–16]. Among these combinations, most photocatalysts are UV-light active (using less than 5% of the solar light spectrum); the low quantum yield of these photocatalysts limits their use in practical applications.

Over the last several decades, hematite (Fe_2O_3) has shown a great potential as a photocatalyst, due to its remarkable performance in PEC water splitting, as well as water purification applications [17]. Its interesting properties, such as a visible bandgap energy (ranging from 1.9 to 2.2 eV), excellent environmental compatibility, low-cost production, and high chemical stability in aqueous solutions, make it applicable in different fields, including photocatalysis, lithium-ion batteries, supercapacitors, and gas

sensors [18,19]. Particularly, its magnetic properties are useful with regard to its easy recyclability and high durability [20]; how-ever, Fe_2O_3 is limited by a high rate of photogenerated charge carriers due to its low carrier mobility (<1 cm^2 V^{-1} s^{-1}), short hole-diffusion length (~2–4 nm), short excited state lifetime (~10 ps), and low absorption coefficient, which significantly reduce its pho-tocatalytic activity performance [21,22]. Attempts have been made to address these issues; for example, Fe_2O_3 has been combined with other semiconductor/carbonaceous materials, doped with met-als and grown with different nanostructures [23]. Fe_2O_3-based heterogeneous photocatalysts exhibited a significant reduction in recombination losses, as well as excellent photocatalytic activity [24]. Despite these results, efforts to further improve the pho-tocatalysis performance of Fe_2O_3 continue. More recently, the polymeric, metal-free semiconductor, and g-C_3N_4, have received much attention, due to its outstanding properties, which include the most stable allotrope phase of carbon, a visible band-gap energy (2.7 eV), stability, viability for hydrogen and oxygen production, and that it consists of only carbon and nitrogen, which are readily available [25,26]. Additionally, its conduction band level is more negative than that of Fe_2O_3, and the visible band gap energy of g-C_3N_4 facilitates high visible light absorption and effective sepa-ration and transportation of photoelectrons [27].

Ye et al. reported, magnetically separable Fe_2O_3/g-C_3N_4 com-posite photocatalysts that exhibited nearly twofold the efficiency of a pure g-C_3N_4 photocatalyst [28]. Liu et al. synthesized a Fe_2O_3/g-C_3N_4 photocatalyst with a nanosheet-like morphology; this photocatalyst demonstrated 70× higher PEC water-splitting performance, compared with that of the Fe_2O_3 photocatalyst, due to its effective separation of photogenerated charge carri-ers [29]. Theerthagiri et al. reported the rapid photodegradation of direct red 81 (DR 81) textile pollutants using Fe_2O_3/g-C_3N_4; the improved performance of this composite was attributed to its high visible light absorption and low recombination [30]. Thus, the Fe_2O_3/g-C_3N_4 hybrid photocatalyst shows a great potential as an efficient photocatalyst. Nevertheless, the achieved performance in the above-mentioned studies is insufficient for commercial devices, possibly due to the low specific surface area and poor visible light absorption. Moreover, the synthesis methods are complicated and require a high temperature, which tends to cause photocatalyst agglomeration. Hence, it is essential to adopt a low-temperature, cost-effective process for Fe_2O_3/g-C_3N_4 photocatalysts, and to fur-ther improve a photocatalytic activity using a large surface area and high visible light absorption.

Despite the proven performance of heterogeneous photocat-alysts, in recent years, there has been increasing interest in plasmonic nanostructures [31]. Noble metal nanoparticles (Au, Ag, Pt, and Pd) exhibit a surface plasmon resonance (SPR) effect that increases substantially the light absorption, leading to enhanced photocatalytic activity [32,33]. With this effect, the metal particles act as electron sinks, resulting in rapid separation and transporta-tion of charge carriers. Thus, we have explored the combination of these two strategies (i.e., semiconductor/semiconductor and metal/semiconductor heterostructure fabrication) in an attempt to create high visible light absorbance and rapid separation of pho-togenerated charge carriers. In the present work, we describe our investigation of Au/g-C_3N_4/Fe_2O_3 hybrid photocatalysts with high visible light absorbance and the larger specific surface area via the plasmonic properties of Au nanoparticles and dispersion of g-C_3N_4 sheets, respectively; to our knowledge, this is the first report on this photocatalytic material. Hybrid photocatalysts were obtained using a simple ultrasonication method at room temperature. The photocatalytic activity was evaluated with respect to the degrada-tion of rhodamine B (RhB) dye under visible irradiation. Moreover, we explored the effect of Au particles size on photocatalytic perfor-mance of g-C_3N_4/Fe_2O_3 hybrid. Our results indicated a significantly

better performance for the Au/g-C_3N_4/Fe_2O_3 hybrid, compared with that of the bare Fe_2O_3 and g-C_3N_4 samples. Finally, we propose a possible photocatalysis mechanism and electron transportation with PEC, supported by optical absorbance results.

2. Experimental details

2.1. Materials

Iron chloride, hexamethylenetetramine (HMTA), urea, sodium sulfide, and RhB were purchased from Junsei Chemical, Japan. Gold chloride was obtained from Sigma–Aldrich. These chemicals were used for synthesis without further purification.

2.2. Synthesis of α-Fe_2O_3 rhombohedra

Rhombohedral-shaped α-Fe_2O_3 was synthesized as reported in our previous work [34]. In brief, a growth solution was prepared by dissolving iron chloride ($FeCl_3$:$6H_2O$, 0.5 M) and hexamethylenete-tramine (HMTA) ($C_6H_{12}N_4$, 0.5 M) in 50:50 vol% solution of absolute ethanol and water. The prepared solution was stirred for 30 min at room temperature to dissolve the precursor powder. Subsequently, a deep red-colored solution was transferred into a Teflon-lined stainless steel autoclave and subjected to heating for 5 h at 150 °C. After completion of the reaction, the autoclave was allowed to cool at room temperature. The solution was then filtered and washed with ethanol several times. Finally, the filtrate was dried at room temperature overnight and was used for analysis and photocataly-sis measurements.

2.3. Synthesis of Au nanoparticles

A colloidal solution of Au nanoparticles was first prepared using the well-known Turkevich method [35]. A 300-mL aque-ous solution of $HAuCl_4$ (0.005 M) was heated until it began to boil. Simultaneously, a 30-mL solution of $Na_3C_6H_5O_7$ (0.04 M) was pre-pared and added to the above solution as soon as boiling was initiated. Immediately, the color of the solution became transparent and then turned pale red, indicating the formation of Au nanopar-ticles having a diameter of only a few nanometers. The diameter of nanoparticles was controlled by adding different amount of tri-sodium citrate (TSC) into gold chloride solution. The average particle size (~12 nm for 60 mL TSC, ~20 nm for 30 mL TSC, and ~26 nm for 15 mL TSC) was confirmed from optical absorbance and transmission electron microscopy (TEM) analysis (Figs. S1 and S2). The prepared Au colloidal solution was used to sensitize hematite nanostructures.

2.4. Synthesis of g-C_3N_4/α-Fe_2O_3 hybrids

Initially, two-dimensional (2-D) sheets of g-C_3N_4 powder were synthesized as reported previously [36]. In short, 20 g of urea was loaded into an alumina crucible and heated at 600 °C for 2 h at a rate of 5 °C (room temperature to 600 °C takes 2 h) using a muf-fle furnace. The furnace was allowed to cool at room temperature naturally. After completion of the process, the yellow-colored pow-der obtained was collected. The g-C_3N_4 sheets were exfoliated by ultrasonciation for 5 h at room temperature and used in combina-tion with hematite. To fabricate the g-C_3N_4/Fe_2O_3 hybrids, g-C_3N_4 powder was mixed in a growth solution of α-Fe_2O_3 (the same solu-tion used to make hematite) before the hydrothermal process and same procedure was repeated to collect powders of g-C_3N_4/Fe_2O_3 hybrid samples. For optimization, we varied loading of g-C_3N_4 such as 0.05 g, 0.10 g, 0.25 g, 0.50 g, and 1.00 g with same amount of R-

hematite precursors, and the obtained samples were represented as $FCN_{0.05}$, $FCN_{0.10}$, $FCN_{0.25}$, $FCN_{0.50}$, and $FCN_{1.00}$, respectively.

2.5. Synthesis of $Au/g\text{-}C_3N_4/\alpha\text{-}Fe_2O_3$ hybrids

Hybrids of $Au/g\text{-}C_3N_4/\alpha\text{-}Fe_2O_3$ were synthesized at room temperature using ultrasonication. $g\text{-}C_3N_4/Fe_2O_3$ powder (50 mg), collected in the experiments described above, was added to 25 mL of Au solution and sonicated for 2 h. After this, the solution was filtered and dried in an oven at 60 °C. This procedure was repeated several times to collect powders of the $Au/g\text{-}C_3N_4/\alpha\text{-}Fe_2O_3$ hybrid for analysis and testing of photocatalytic activity. Other two Au nanoparticle sizes were also sensitized using the same process. The samples sensitized with Au nanoparticles are represented as $A_{26}FCN_{0.50}$, $A_{20}FCN_{0.50}$, $A_{12}FCN_{0.50}$, for 26, 20, and 12 nm, respectively. Consequently, we fabricated 12 nm-sized Au sensitized $g\text{-}C_3N_4$ hybrid, and that powder was collected by repeating same procedure and presented as ACN. For better comparison, the same hybrid sample was prepared mechanically as follows; powders of hematite and $g\text{-}C_3N_4$ were added in Au solution simultaneously and stirred at room temperature for 1 h. Then solution was filtered and the obtained powders were used for photocatalysis degradation. The mechanically prepared sample was presented as $AFCN_M$.

2.6. Analysis instruments

The phase formation of pure R-hematite and its hybrids having an Au and $g\text{-}C_3N_4$ structure, were analyzed using X-ray diffraction (XRD, Rigaku D/MAX-2500/PC, Cu-Kα, λ = 1.5418 Å) over the range of 10–70°. The microstructures of synthesized photocatalysts were studied by field-emission scanning electron microscopy (FE-SEM, Hitachi S4800, 15 kV) and TEM (JEOL 2100, 200 kV). Fourier transform infrared (FTIR) spectra were recorded over the range from 4000 to 400 cm^{-1} using KBr pellets at room temperature. The Brunauer–Emmett–Teller (BET) was used to measure specific surface area of all photocatalysts by nitrogen adsorption–desorption isotherms using a Quantochrome system (Autosorb iQ-C, Quantachrome instruments, USA) cooled to liquid nitrogen temperatures (AS1). The total pore size distribution was determined using the Barret–Joyner–Halender (BJH) method. The chemical composition of the ternary hybrid sample was determined using X-ray photoelectron spectroscopy (XPS, Sigma Probe; Thermo-Scientific, UK). Ultraviolet–vis (UV–vis) diffuse reflectance spectra of the powder samples were measured using a UV–vis spectrophotometer integrated with a diffused reflectance accessory (V-650, Jasco, Japan); a $BaSO_4$ bar was used as a standard reference.

2.7. Photoelectrochemical (PEC) measurements

Photocurrent generation and open-circuit voltage decay measurements were performed on a potentiostat (VersaSTAT 4, Princeton Applied Research, USA) using a standard three-electrode system. The working electrode consisted of fluorine-doped tin oxide (FTO) deposited with photocatalysts using a Liquion solution (Ion Power, Inc., UK) (1×1 cm^2). A platinum wire was used as the counter-electrode, and Ag/AgCl (3 M KCl) was used as the reference electrode. The electrolyte was an aqueous sodium sulfide (0.5 M) solution. For photoresponse measurements, the electrochemical cell was irradiated repeatedly over several cycles with a halogen lamp (incident power: 5 mW cm^{-2}).

2.8. Photocatalytic activity

The visible-light photocatalytic activity of the synthesized catalysts was evaluated by RhB degradation (4 mg L^{-1} in water) in a

batch-type reactor. A halogen lamp was used as the visible light source. For the photocatalytic test, 50 mg of catalyst powder was dispersed in 250 mL of RhB solution; the solution was then stirred magnetically in the dark for 1 h before actual measurement to achieve equilibrium adsorption of the catalyst and dye molecules. During irradiation, 3 mL of the suspension solution was collected at regular time intervals and centrifuged to separate the catalyst particles. The RhB concentration was monitored by measuring the change in the optical density at 554 nm in the UV–vis spectra.

3. Results and discussion

3.1. XRD

Fig. 1 shows XRD patterns of grown $\alpha\text{-}Fe_2O_3$ and its hybrids with $g\text{-}C_3N_4$ sheets and Au nanoparticles; the vertical line at the bottom corresponds to the Joint Committee on Powder Diffraction Standards (JCPDS) data for hematite (PDF#01-076-4579, blue lines) and Au (PDF#98-000-0230, red lines) as a reference. For the pure $\alpha\text{-}Fe_2O_3$ sample, all of the diffraction peaks in the pattern matched the rhombohedral phase of hematite, thus, confirming successful formation of a pure hematite. Further, XRD pattern of pure $g\text{-}C_3N_4$ exhibits two peaks at 13.1° and 27.8°, indicating the formation of phase pure $g\text{-}C_3N_4$ structure. Particularly, intense peak at 27.8° originated from interlayer-stacking, confirms the graphitic structure of $g\text{-}C_3N_4$ sheets [37]. The patterns of $g\text{-}C_3N_4/Fe_2O_3$ hybrids show peaks corresponding to R-hematite as well as $g\text{-}C_3N_4$ structure, which illustrates the formation of hybrid photocatalysts. Interestingly, introduction of $g\text{-}C_3N_4$ with different amount i.e., 0.05–1.00 g did not seem to have any effect on crystal structure of R-hematite. The peak of $g\text{-}C_3N_4$ at 27.8° becomes dominant for larger amount i.e., $FCN_{1.00}$ as compared with that of $FCN_{0.05}$ sam-
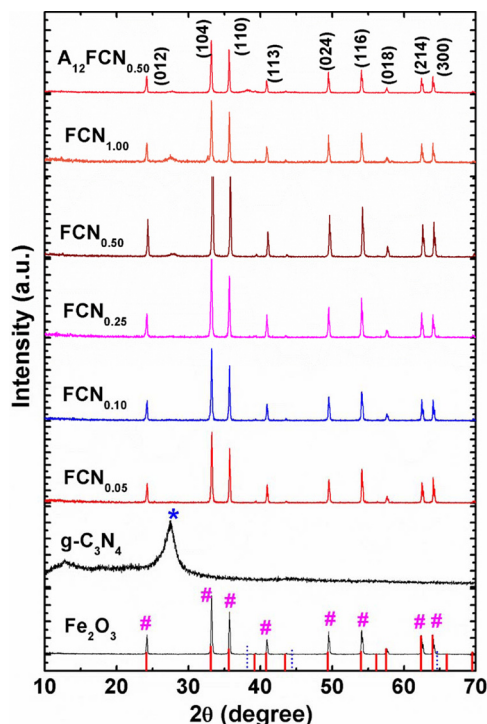
Fig. 1. X-ray diffraction (XRD) patterns of pristine rhombohedral Fe_2O_3, $g\text{-}C_3N_4$, $FCN_{0.05}$, $FCN_{0.10}$, $FCN_{0.25}$, $FCN_{0.50}$, $FCN_{1.00}$, and $A_{12}FCN_{0.50}$ hybrid samples. For comparison, Joint Committee on Powder Diffraction Standards data for Au (PDF#98-000-0230) and Fe_2O_3 (PDF#01-076-4579) are given in the vertical lines in the bottom pattern (solid blue lines = Fe_2O_3, dotted red lines = Au). (For interpretation of the references to color in this figure legend, the reader is referred to the web version of this article.)

ple. Similarly, after Au (12 nm in diameter) sensitization, no obvious change in the diffraction pattern was revealed; this indicated that Au had no effect on the crystalline structure of hematite and g-C_3N_4. The two low intensity peaks at 38.18 and 44.38° indicated the presence of metallic Au nanoparticles in the sample. Hence, the existence of diffraction peaks related to the Au, g-C_3N_4, and α-Fe_2O_3 phases, proved successful formation of ternary hybrids using a sonication method at room temperature. The low intensity of the Au and g-C_3N_4 phases was attributed to the presence of a relatively low amount of the amorphous phase of these materials.

3.2. FE-SEM and TEM

The microstructural features of pure Fe_2O_3 and its hybrids with Au and g-C_3N_4 were examined by FE-SEM analysis. Fig. 2A shows the rhombohedral-like shape of the Fe_2O_3 structure, with a few random nanoparticles distributed throughout the sample area. The magnified image revealed a smooth surface for the rhombohedral shape (average size: 100–150 nm). The growth of the rhombohedral shape was attributed to the presence of HMTA in the solution during the hydrothermal process. It is known that HMTA supplies OH^- ions slowly during $FeCl_3$ hydrolysis at elevated temperatures [38–40]. Additionally, the amine group in HMTA acts as a structural directing agent. Thus, HMTA retarded the growth of hematite Fe_2O_3 on specific surfaces, leading to the rhombohedral-like shape. After the growth of the hematite nanostructures, these structures were combined with either Au (12 nm) or g-C_3N_4 for enhanced photocatalysis. FE-SEM images of pure g-C_3N_4 network are shown in Fig. 2B. It is clearly seen that the porous structure of graphitic carbon nitride was formed throughout the sample. The magnified image shows the g-C_3N_4 sheets with an average thickness of few nanometers, distributed uniformly. For $FCN_{0.05}$ hybrid, most of sample area covered with hematite rhombohedra and g-C_3N_4 sheets were distributed sporadically (Fig. 2C). This could be resulted from relatively low amount of g-C_3N_4 in the hybrid sample. As we increased g-C_3N_4 loading to 0.10 g for $FCN_{0.10}$, the wrapping of rhombohedra was found to be more comparable with that of former sample. Further, with increment in g-C_3N_4 loading, the most of rhombohedra were wrapped with g-C_3N_4 sheets and also covered large area of sample (Fig. 2D–G). It was found to be maximum for $FCN_{1.00}$ hybrid compared with that of all hybrid samples. Finally, the Au(12 nm)/g-C_3N_4/Fe_2O_3 hybrid revealed the presence of Au nanoparticles, as well as g-C_3N_4 sheets, distributed throughout the entire sample, combining uniformly with the rhombohedral structure (Fig. 2H); the magnified FE-SEM image clearly shows the existence of Au and g-C_3N_4 sheets tethered to the rhombohedral structure of hematite. The relative size of Au nanoparticles was found to be low compared with that of rhombohedra structure. Thus, FE-SEM analysis confirmed the formation of a ternary hybrid consisting of Au, g-C_3N_4, and Fe_2O_3 nanostructures.

The detailed morphology, shape, and formation of pure and hybrid photocatalysts were studied using TEM. Fig. 3A shows TEM images of an Fe_2O_3 sample, revealing a significant amount of rhombohedral shape formation, as well as particles having a random shape. High-resolution TEM images in the magnified image of Fig. 3A show the growth of the single rhombohedral shape (average length: 80 nm; average width: 80 nm). This confirms the growth of the rhombohedral hematite structure using a hydrothermal method.

For the g-C_3N_4/Fe_2O_3 ($FCN_{0.50}$) hybrid, the rhombohedral structure was dispersed on the surface of the micrometer-sized g-C_3N_4 sheets (Fig. 3B). Almost the entire area of the g-C_3N_4 sheets was covered with the Fe_2O_3 rhombohedral shape, without aggregation or modification in size (magnified image of Fig. 3B); this result was similar to the contents of FE-SEM images.
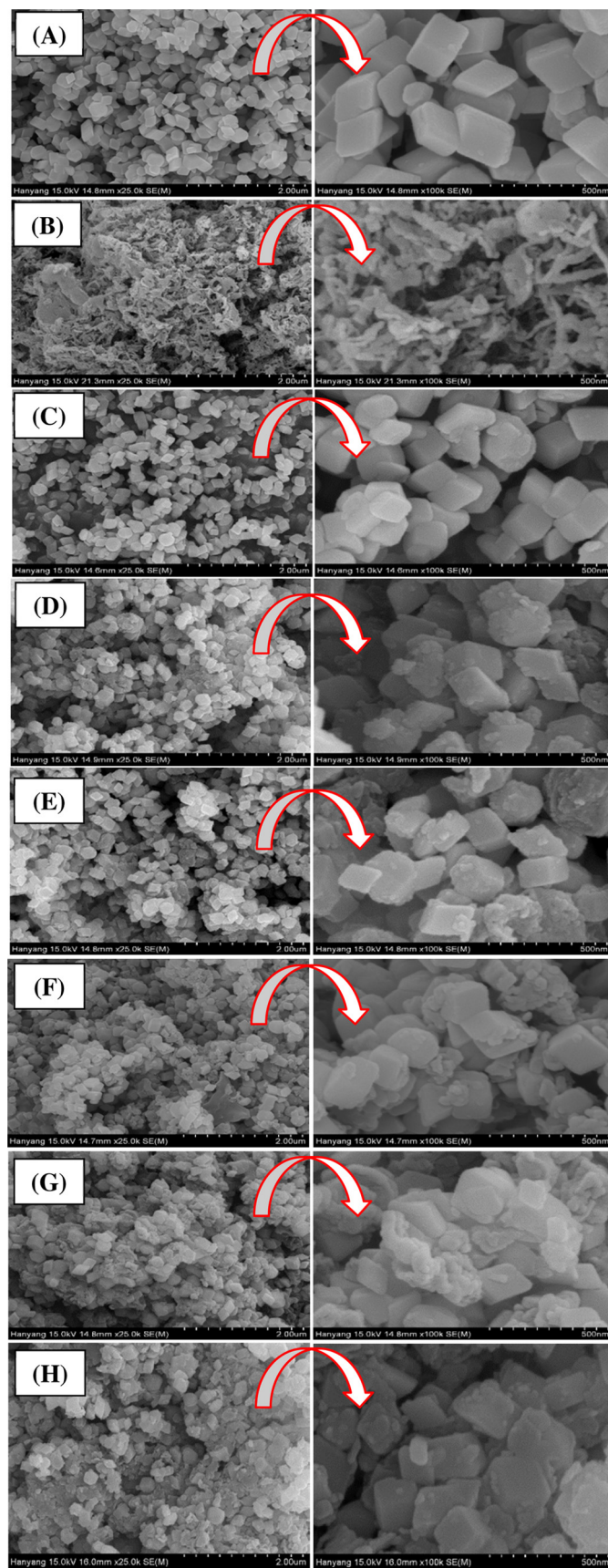
Fig. 2. Field-emission scanning electron microscopy (FE-SEM) images of (A) the rhombohedral structure of pristine Fe_2O_3, (B) g-C_3N_4, (C) $FCN_{0.05}$, (D) $FCN_{0.10}$, (E) $FCN_{0.25}$, (F) $FCN_{0.50}$, (G) $FCN_{1.00}$, and (H) $A_{12}FCN_{0.50}$. All images are recorded at 25× (left side images) and 100× (right side images).
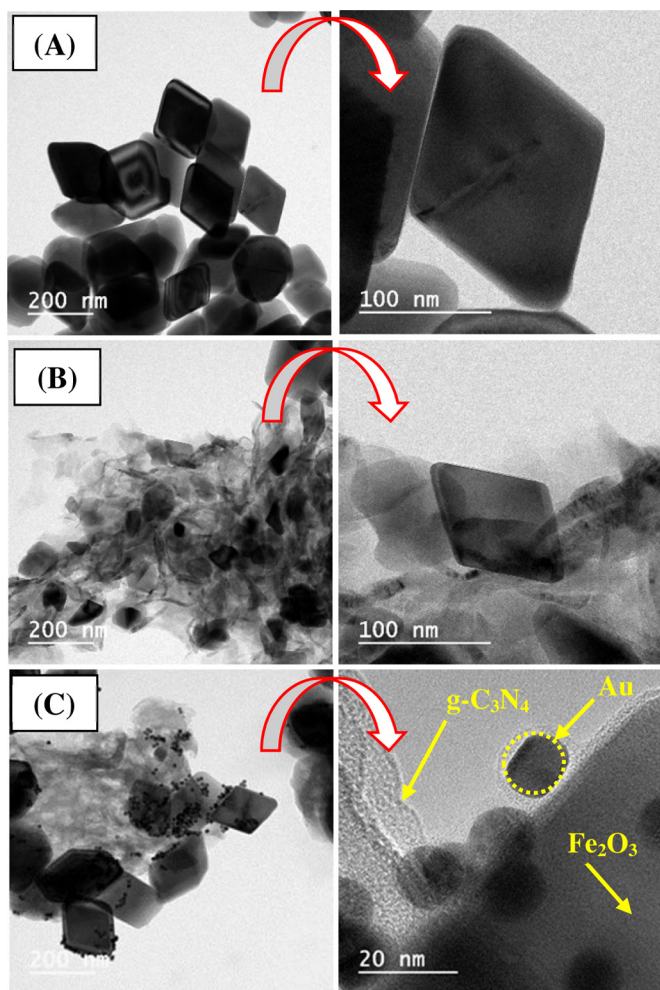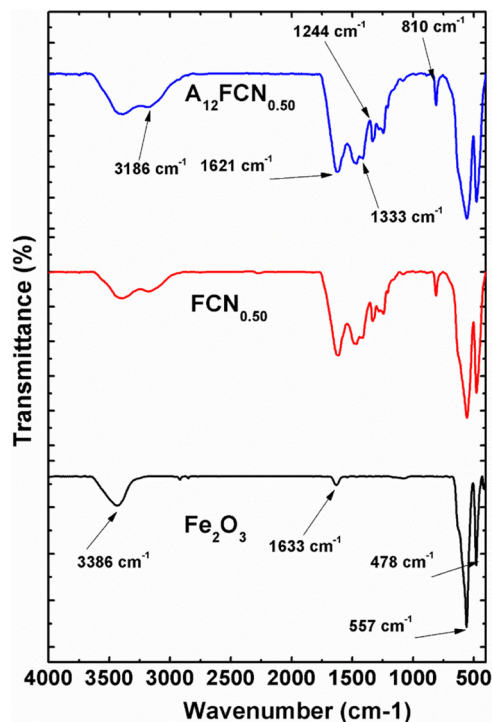
Fig. 3. Transmission electron microscopy (TEM) images of selected sample; (A) the rhombohedral structure of pristine Fe_2O_3, (B) $FCN_{0.50}$, and (C) $A_{12}FCN_{0.50}$ hybrid samples. The corresponding magnified TEM images are provided to the right of the figures.
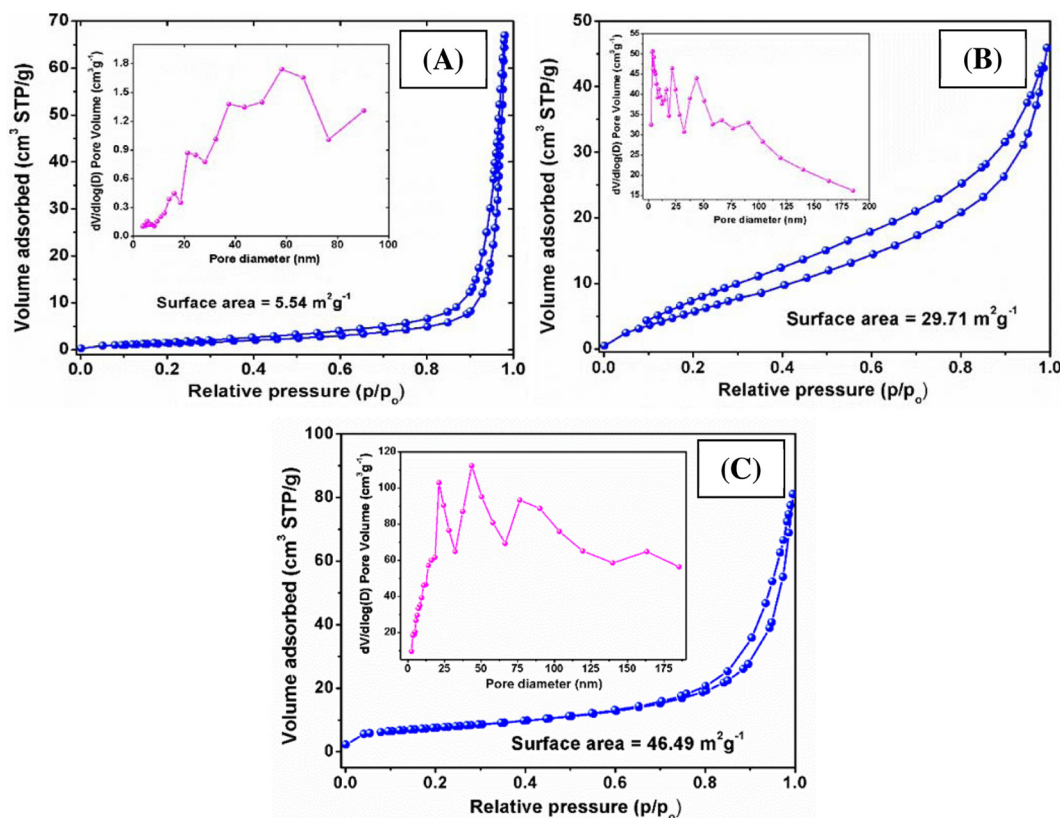

Fig. 4. Fourier transform infrared (FTIR) spectra of selected sample i.e., (A) the rhombohedral structure of pristine Fe_2O_3, (B) $FCN_{0.50}$, and (C) $A_{12}FCN_{0.50}$ hybrid samples.

TEM images of the Au(12 nm)/g-C_3N_4/Fe_2O_3 hybrid sample are shown in Fig. 3C. The rhombohedral hematite and Au particles were uniformly distributed throughout the sample and covered almost the entire area of the g-C_3N_4 sheets. The magnified TEM image revealed small Au particles on the rhombohedra, as well as g-C_3N_4 sheets (magnified image in Fig. 3C); these results clearly show the successful formation of ternary hybrids, which may improve the photocatalytic activity of pristine hematite nanostructures.

3.3. FTIR analysis

To understand the chemical bonding mechanism among hematite, g-C_3N_4/Fe_2O_3, and Au/g-C_3N_4/Fe_2O_3 hybrids, we recorded the FTIR spectra of pristine and hybrid samples. In Fig. 4, the bottom curve shows the spectrum of pure hematite and detailed wavenumbers for the corresponding bands. For pure hematite, two characteristic bands at 478 and 557 cm^{-1} were assigned to stretching and bending modes of the Fe—O bond [41]. Moreover, the two bands at 3386 and 1633 cm^{-1} corresponded to asymmetrical stretching and deformation vibration, respectively, of adsorbed H_2O molecules on the hematite surface [42]. For the g-C_3N_4 incorporated sample $FCN_{0.50}$, three additional bands at 1621, 1244, and 1233 cm^{-1} were evident in the spectra; these bands corresponded to the breathing mode of s-triazine and C—N for the C=N bonds in the g-C_3N_4 network [43,44]. Moreover, two major bands associated

with the hematite structure were observed. For the Au(12 nm)/g-C_3N_4/Fe_2O_3 hybrid sample, a similar trend was evident, indicating that Au had no obvious effect on the bonding between the g-C_3N_4 and Fe_2O_3 structures. Additionally, the two bands at 3186 and 810 cm^{-1}, common to both the g-C_3N_4/Fe_2O_3 and Au(12 nm)/g-C_3N_4/Fe_2O_3 hybrids, were assigned to defect sites; these defects were located in the aromatic ring with the NH groups and the out-of-plane skeletal modes of the triazine cycles [45]. Thus, taken together, these results revealed strong interactions within the hybrid samples.

3.4. Surface area and pore size distribution analysis

To determine the effect of Au and g-C_3N_4 introduction on the surface properties of Fe_2O_3 nanostructures, we measured the nitrogen adsorption–desorption isotherms and the BJH pore size distribution of pure and hybrid samples (Fig. 5A–C). All apparent curves followed the H_3 hysteresis nature, with a type-IV isotherm, which revealed the presence of mesopores in the samples. The calculated specific surface areas (S_{BET}) of pure Fe_2O_3, $FCN_{0.50}$, and $A_{12}FCN_{0.50}$ samples, were 5.5, 29.7, and 46.5 $m^2\,g^{-1}$, respectively. The obtained surface area value for Au(12 nm)/g-C_3N_4/Fe_2O_3 was almost nine-fold higher than that of pure Fe_2O_3 and much more comparable with that of the g-C_3N_4/Fe_2O_3 hybrid samples. Therefore, the loading of Au and g-C_3N_4 had a synergetic effect on the S_{BET} of the pure Fe_2O_3 nanostructure; this could be beneficial with respect to improving photocatalytic performance. Using the BJH method, the calculated pore size exhibited a broader distribution over the range 10–50 nm, indicating the existence of strong interactions among the Au, g-C_3N_4, and Fe_2O_3 nanostructures. These pores provided effective transport pathways for RhB molecule adsorption, enhancing photocatalytic performance.

Fig. 5. Nitrogen adsorption–desorption isotherms and Brunauer–Emmett–Teller (BET) specific surface area of (A) the rhombohedral structure of pristine Fe_2O_3, (B) $FCN_{0.50}$, and (C) $A_{12}FCN_{0.50}$ hybrid samples. The inset shows the corresponding pore size distribution curves plotted using the Barret–Joyner–Halender (BJH) method.

3.5. XPS analysis

The existence and oxidation state of composite materials in the $Au(12\,nm)/g\text{-}C_3N_4/Fe_2O_3$ hybrid sample were examined using XPS spectra. The survey spectra exhibited distinctive peaks corresponding to iron (Fe), oxygen (O), carbon (C), nitrogen (N), and Au elements, confirming the formation of a ternary hybrid photocatalyst (Fig. 6A). For quantitative analysis of Fe 2p, the XPS spectrum of Fe 2p was deconvoluted into seven multiplet peaks (Fig. 6B). The strongest peaks at 710.06 and 723.22 eV were assigned to the binding energies of the Fe $2p_{3/2}$ and Fe $2p_{1/2}$ levels. The peak at 712.01 eV demonstrated the hydroxyl groups bonded with Fe^{3+} cations in the hematite phase [46]. The peak at the binding energy of 714.17 eV may be associated with $\alpha\text{-}Fe_2O_3$ [47]. Two peaks centered at binding energies of 716.62 and 719.43 eV were related to the satellite peaks revealed for the hematite nanostructures. Finally, the two additional peaks centered at 723.22 and 725.62 eV indicated the presence of the Fe^{3+} state usually found in $\alpha\text{-}Fe_2O_3$ [48].

Four different peaks were observed for the O 1s core level spectra (Fig. 6C). The first one at a binding energy of 529.21 eV was attributed to lattice O^{2-} ions in the $\alpha\text{-}Fe_2O_3$ phase, which confirmed the presence of the hematite phase in the hybrid sample. The three peaks at 531.22, 533.03, and 534.59 eV corresponded to oxygen defects in the hematite matrix (OH^-, C=O, or C—O) and moisture adsorption on the hematite surface; i.e., H_2O [49–51]. Moreover, the relatively strong peak at 531.22 eV indicated the presence of the hydroxide phase of hematite [52].

The core-level XPS spectra of C 1s exhibited four distinct peaks (Fig. 6D). The strongest peak at 286.19 eV originated from a triazine ring in hybridized carbon [53]. A comparatively low-intensity peak at 284.59 eV indicated the presence of carbon nitride with a low graphitic value [54]. The two peaks at 288.45 and 290.04 eV were allocated to the C—N—C network and π–π^* transitions in the $g\text{-}C_3N_4$ matrix [55].

Gaussian fitting of the N 1s spectra revealed an asymmetrical feature with three distinguishable peaks (Fig. 6E). The first and strongest peak at 400.15 eV was attributed to bridging nitrogen atoms of tertiary nitrogen; i.e., $N\text{-}(C)_3$, indicating a large amount of urea polymerization [56]. The two comparatively low-intensity peaks, located at 398.15 and 401.86 eV, were attributed to sp^2 nitrogen and N=H groups in the $g\text{-}C_3N_4$ network [57].

High-resolution Au 4f core-level XPS spectra showed two major characteristic peaks at binding energies of 84.83 and 86.84 eV, attributed to Au $4f_{5/2}$ and Au $4f_{7/2}$ bands, respectively (Fig. 6F); this confirmed the presence of Au in the form of an Au^0 valence (i.e., metallic) state [58]. Additionally, a small peak was observed at 90.29 eV, which was assigned to the oxidized Au^+ state [59].

3.6. Optical absorption properties

The optical absorbance of the synthesized photocatalysts was studied by measuring the UV–vis absorbance spectra over the range from 400 to 850 nm (Fig. 7). The sharp absorption edge at around 450 nm was resulted from band gap energy of $g\text{-}C_3N_4$ structure. For hematite, the existence of a strong absorption edge near 575 nm was attributed to the band-gap energy absorption of the hematite structure [60]. Compared with pure hematite and $g\text{-}C_3N_4$ structures, the $g\text{-}C_3N_4/Fe_2O_3$ hybrid sample showed enhanced absorbance, particularly in visible region, which was aroused from band gap energy of hematite and $g\text{-}C_3N_4$ structures [61]. The optical absorbance of hybrid sample was further improved with increment of $g\text{-}C_3N_4$ loading than that of former sample and found to be highest for $FCN_{1.00}$ hybrid. To maximize the energy of the visible solar spectrum, we added Au nanoparticles to the $g\text{-}C_3N_4/Fe_2O_3$ hybrid.
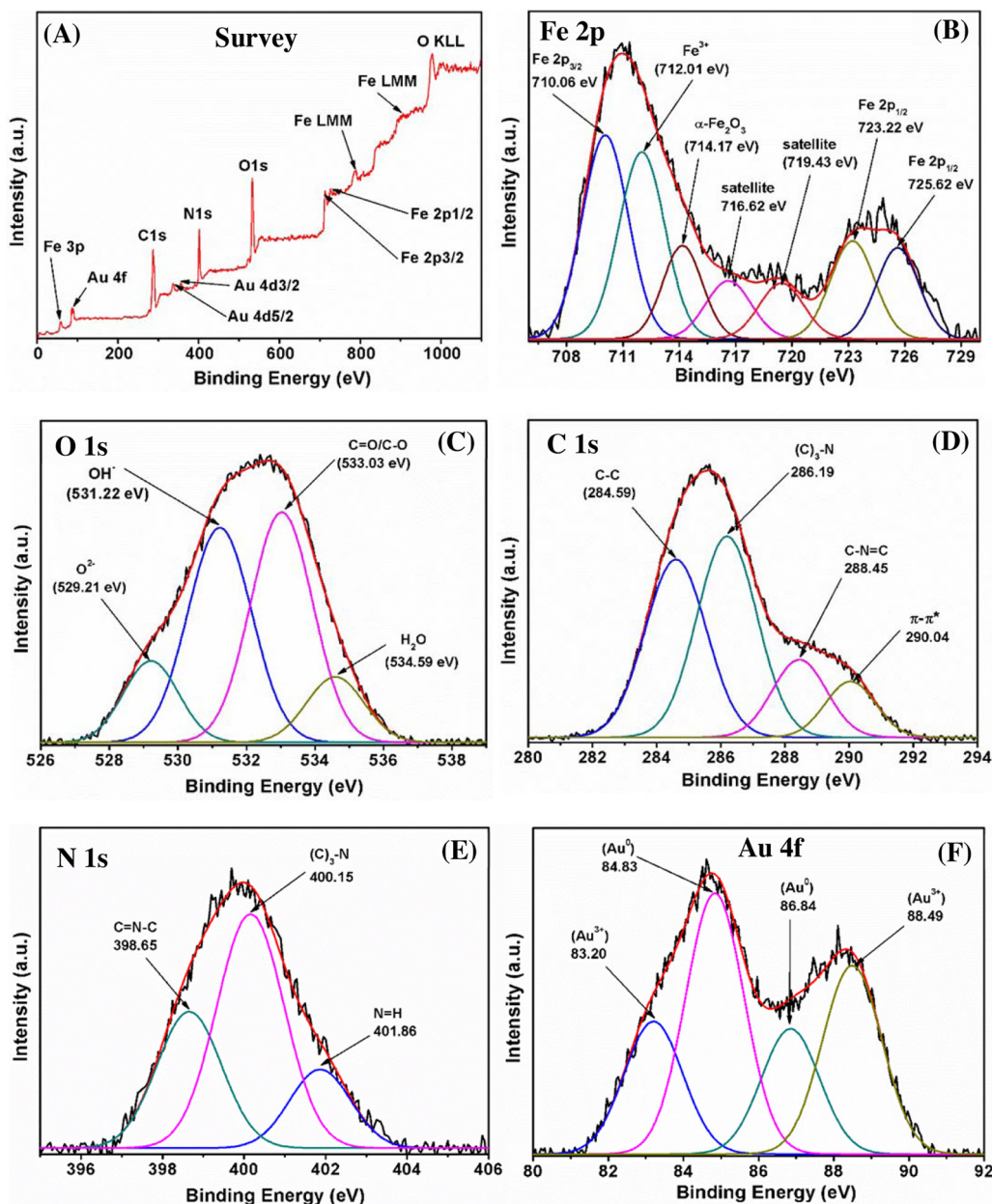
Fig. 6. X-ray photoelectron spectroscopy (XPS) spectra of the Au/g-C$_3$N$_4$/Fe$_2$O$_3$ hybrid photocatalyst: (A) survey spectrum and high-resolution spectra of (B) Fe 2p, (C) O 1s, (D) C 1s, (E) N 1s, and (F) Au 4f.

A significant enhancement was evident in the visible spectrum absorbance for A$_{12}$FCN$_{0.50}$ hybrid, compared with pure hematite and the other hybrid samples. Thus, these results illustrate that the introduction of Au and g-C$_3$N$_4$ into the Fe$_2$O$_3$ nanostructure utilized almost the entire visible range of solar light, potentially, resulting in improved photocatalytic performance.

3.7. Photodegradation of RhB

The photodegradation ability of synthesized pure and hybrid photocatalysts was investigated using photocatalytic decolorization of RhB in an aqueous solution under visible irradiation. To determine the improvement in the photocatalytic activity, we used commercial Degussa powder (P25) as a reference photocatalyst. There are numerous reports of RhB degradation using hematite nanostructures and their hybrids, with different semiconductor photocatalysts. Nevertheless, few studies investigated

binary hybrids based on Au, g-C$_3$N$_4$, and Fe$_2$O$_3$ materials [62,63]. In particular, Au/g-C$_3$N$_4$/Fe$_2$O$_3$ has not been investigated for photodegradation of organic pollutants. This inspired us to assess the photodegradation performance of Au/g-C$_3$N$_4$/Fe$_2$O$_3$ hybrid photocatalysts under visible irradiation.

3.8. Binary hybrids

Fig. 8A–I illustrates that the color of the RhB dye solution collected under the exposure of visible irradiation with increasing time for (A) Fe$_2$O$_3$, (B) g-C$_3$N$_4$, (C) Au/g-C$_3$N$_4$ (ACN) (D) FCN$_{0.05}$, (E) FCN$_{0.10}$, (F) FCN$_{0.25}$, (G) FCN$_{0.50}$, and (H) FCN$_{1.00}$ hybrid samples. The gradual reduction in RhB peak at 554 nm with the exposure of irradiation time, clearly indicated the destruction of RhB molecules. In addition to this, presence of minute hypsochromic shift is found, indicating that the absence of *N*-de-ethylation of RhB. Almost complete degradation of RhB was taking place for most of hybrid
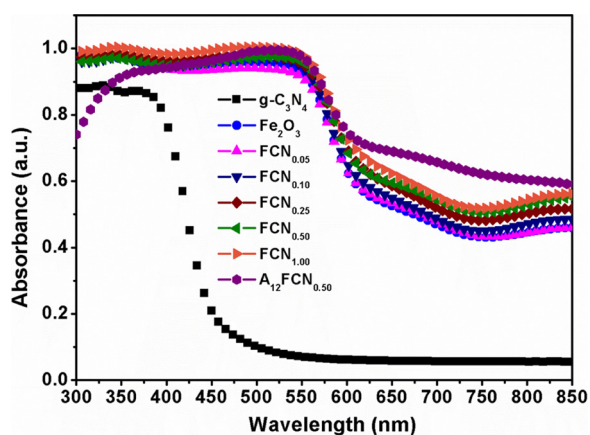
Fig. 7. Ultraviolet–vis (UV–vis) absorption spectra of Fe_2O_3, g-C_3N_4, $FCN_{0.05}$, $FCN_{0.10}$, $FCN_{0.25}$, $FCN_{0.50}$, $FCN_{1.00}$, and $A_{12}FCN_{0.50}$ hybrid samples.

Table 1
The calculated kinetic rate constants (min^{-1}) for Fe_2O_3, g-C_3N_4, ACN, $FCN_{0.05}$, $FCN_{0.10}$, $FCN_{0.25}$, $FCN_{0.50}$, $FCN_{1.00}$, $A_{26}FCN_{0.50}$, $A_{20}FCN_{0.50}$, $A_{12}FCN_{0.50}$, and $AFCN_M$ hybrid photocatalysts samples.

Sample details	Kinetic rate constant $\times 10^{-3}$ (min^{-1})
RhB solution	0.2
P25 (TiO_2)	0.3
Fe_2O_3	1.7
g-C_3N_4	2.3
ACN	2.6
$FCN_{0.05}$	8.0
$FCN_{0.10}$	9.7
$FCN_{0.25}$	12.8
$FCN_{0.50}$	16.6
$FCN_{1.00}$	14.0
$A_{26}FCN_{0.05}$	17.7
$A_{20}FCN_{0.05}$	26.6
$A_{12}FCN_{0.05}$	31.6
$AFCN_M$	4.9

Values for P25 and RhB solution under visible irradiation are also given for reference.

samples. Particularly, $FCN_{0.50}$ hybrid degrades RhB within 90 min, which is the minimum time required for degradation. Regardless, pristine hematite and g-C_3N_4 structure and other hybrid samples require more than 120 min. This clearly showed that g-C_3N_4 has synergetic effect on photocatalytic activity of hematite structure.

The photocatalytic activity of pure and hybrid samples was further analyzed by plotting the relative absorbance of 100 $A_0/A(t)$, where A_0 is the absorbance before irradiation, and $A(t)$ is the absorbance of the dye solution as a function of the irradiation time (Fig. 9A). Without a catalyst, a slight decrease in the RhB concentration was observed after visible irradiation. On the contrary, the RhB concentration decreased remarkably in the presence of catalysts. The g-C_3N_4/Fe_2O_3 hybrid with 0.500 g of g-C_3N_4 showed higher performance than did the other hybrids and pure hematite. Consequently, Au nanoparticle sensitized g-C_3N_4 also exhibited better performance as compared with that of pure g-C_3N_4 network. Hence, it was observed that adding g-C_3N_4 to the hematite and Au (12 nm) to g-C_3N_4 nanostructures had a positive effect on photocatalytic activity; this may be attributed to enhanced charge separation and minimal recombination losses, compared with that of pure hematite.

The photodegradation properties of the materials were analyzed by calculating the kinetic rate constant from $\ln(A_0/A(t))$ versus t, where k is the gradient of this curve; i.e., the apparent kinetic rate constant. The linear curve shown in Fig. 9B indicates that first-order reaction kinetics were applicable, which follow the Langmuir–Hinshelwood model [64]. The kinetic rate constant for $FCN_{0.50}$ was $k = 16.6 \times 10^{-3}$ min^{-1}, which was almost 8-fold larger than that of pristine hematite ($k = 1.7$ min^{-1}) and was the highest among all Fe_2O_3/g-C_3N_4 based samples. The rate constants of the g-C_3N_4 ($k = 2.3$ min^{-1}), Au/g-C_3N_4 ($k = 2.6$ min^{-1}), $FCN_{0.05}$ ($k = 8.0$ min^{-1}), $FCN_{0.10}$ ($k = 9.7$ min^{-1}), $FCN_{0.25}$ ($k = 12.8$ min^{-1}), and $FCN_{1.00}$ ($k = 14.0$ min^{-1}) were all greater than that of the P25 ($k = 0.3$ min^{-1}) powders, but were considerably smaller than that of the $FCN_{0.50}$ hybrid (Table 1). Therefore, we confirmed the better performance of the g-C_3N_4/Fe_2O_3 hybrid sample with optimum 0.500 g of g-C_3N_4 powder for photodegradation applications.

3.9. Ternary hybrids

Fig. 10A–D shows optical absorbance of RhB solution degraded using Au and g-C_3N_4 incoporated Fe_2O_3 ternary hybrid photocatalysts i.e., $A_{26}FCN_{0.50}$, $A_{20}FCN_{0.50}$, and $A_{12}FCN_{0.50}$. With this, we prepared Au (12 nm)/g-C_3N_4/Fe_2O_3 ($A_{12}FCN_M$) sample mechanically for better comparison with hydrothermally fabricated hybrid photocatalysts. From Fig. 10D, it is clearly seen that the presence of

RhB peak until 120 min visible irradiation, which reveals the poor degradation performance as compared with that of hydrothermally fabricated sample. Moreover, we found similar kind of minute shift in RhB peak due to lack of de-ethylation process. Then, the 12 nm Au nanoparticles sensitized g-C_3N_4/Fe_2O_3 hybrid degrades RhB within 50 min, which is the shortest time among all Au-incorporated and mechanically prepared hybrid photocatalysts. Moreover, required time to degrade RhB using $A_{12}FCN_{0.50}$ is less than that of binary hybrids of g-C_3N_4 and Fe_2O_3.

In addition to optical absorbance, relative absorbance of $A_{26}FCN_{0.50}$, $A_{20}FCN_{0.50}$, $A_{12}FCN_{0.50}$, and $A_{12}FCN_M$ hybrids were compared for understanding photocatalytic performance. The relative absorbance of RhB and TiO_2 measured under the same condition, was provided for comparison (Fig. 11A). It is observed that TiO_2 powder and RhB without any catalyst, show almost no degradation. However, Au and g-C_3N_4 introduced $A_{26}FCN_{0.50}$, $A_{20}FCN_{0.50}$, $A_{12}FCN_{0.50}$, and $A_{12}FCN_M$ hybrids showed rapid decrease of RhB peak compared with TiO_2 powder under visible irradiation. More interestingly, among different size of Au sensitized hybrids, the $A_{12}FCN_{0.50}$ exhibited superior activity as compared with $A_{26}FCN_{0.50}$, $A_{20}FCN_{0.50}$, and $A_{12}FCN_M$ hybrids. This is caused by effective separation of electron–hole pairs generated at the interface of Au, g-C_3N_4, and Fe_2O_3 nanostructures. Further, smaller Au particles size shifts Fermi level toward more negative potential, leading to sequential transportation of photoelectrons; and hence, resulting in excellent photocatalytic activity [65,66]. Therefore, we can say that introduction of Au and g-C_3N_4 to Fe_2O_3 nanostructures enhance the charge generation and transportation for superior photodegradation under visible irradiation.

To explore RhB degradation using ternary hybrids, we determined kinetic rate constants of $A_{26}FCN_{0.50}$, $A_{20}FCN_{0.50}$, $A_{12}FCN_{0.50}$, and $A_{12}FCN_M$ hybrids. The linear behavior of logarithmic plots revealed the pseudo-first order reaction during RhB degradation. Among ternary hybrids, the $A_{12}FCN_{0.50}$ ($k = 31.6$ min^{-1}) exhibits the best catalytic activity than that of $A_{26}FCN_{0.50}$ ($k = 17.7$ min^{-1}), $A_{20}FCN_{0.50}$ ($k = 26.6$ min^{-1}), and $A_{12}FCN_M$ ($k = 4.9$ min^{-1}) hybrid photocatalysts. From these results, it is seen that Au and g-C_3N_4 incorporation showed synergistic effect on Fe_2O_3 photocatalytic activity.

3.10. Proposed photocatalysis mechanism

In the present work, the Au/g-C_3N_4/Fe_2O_3 hybrid showed excellent photocatalytic activity, compared with that of pure Fe_2O_3 and the g-C_3N_4 nanostructures. The improvement in performance indicates that Au and g-C_3N_4, in combination with Fe_2O_3,
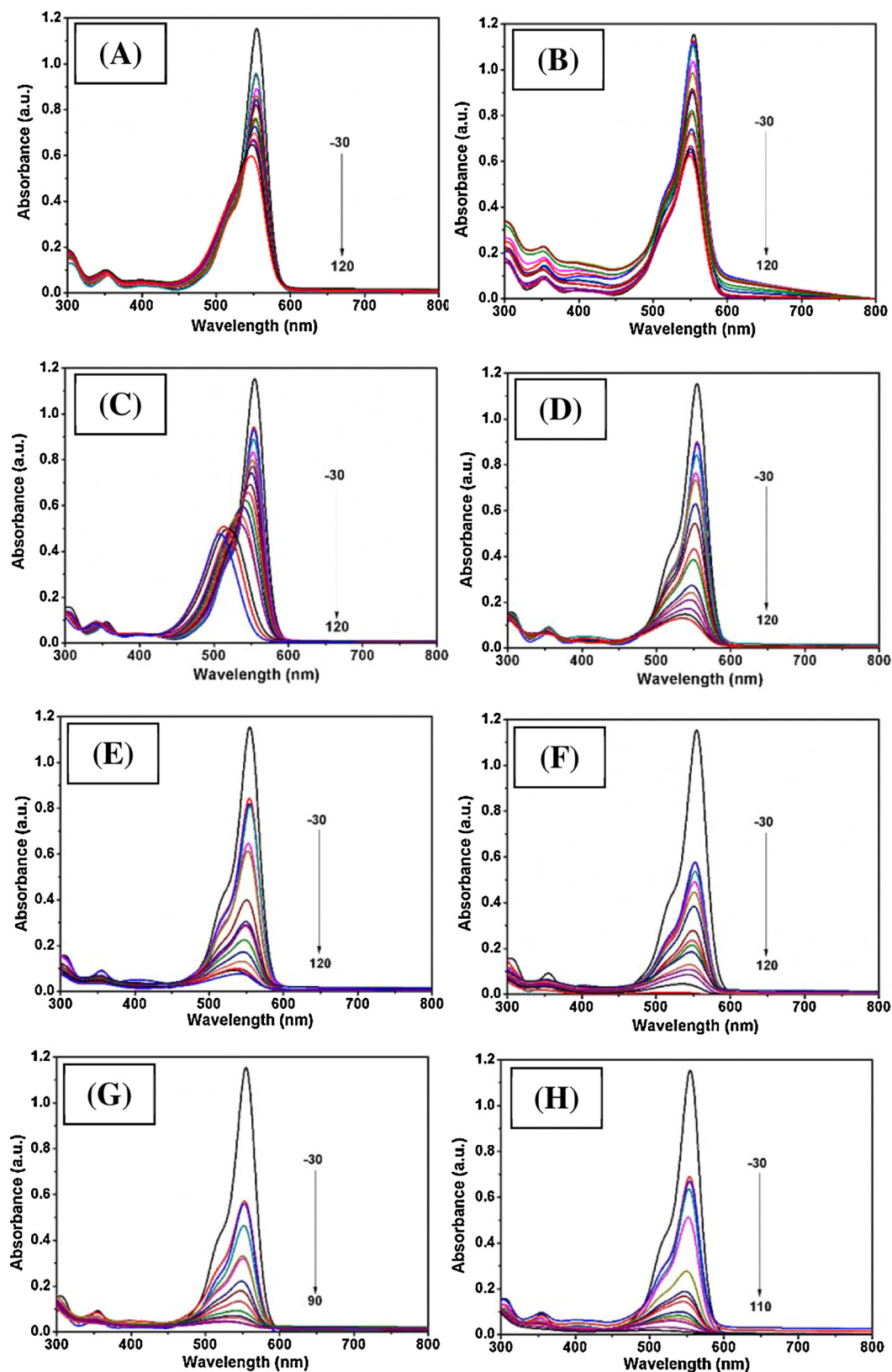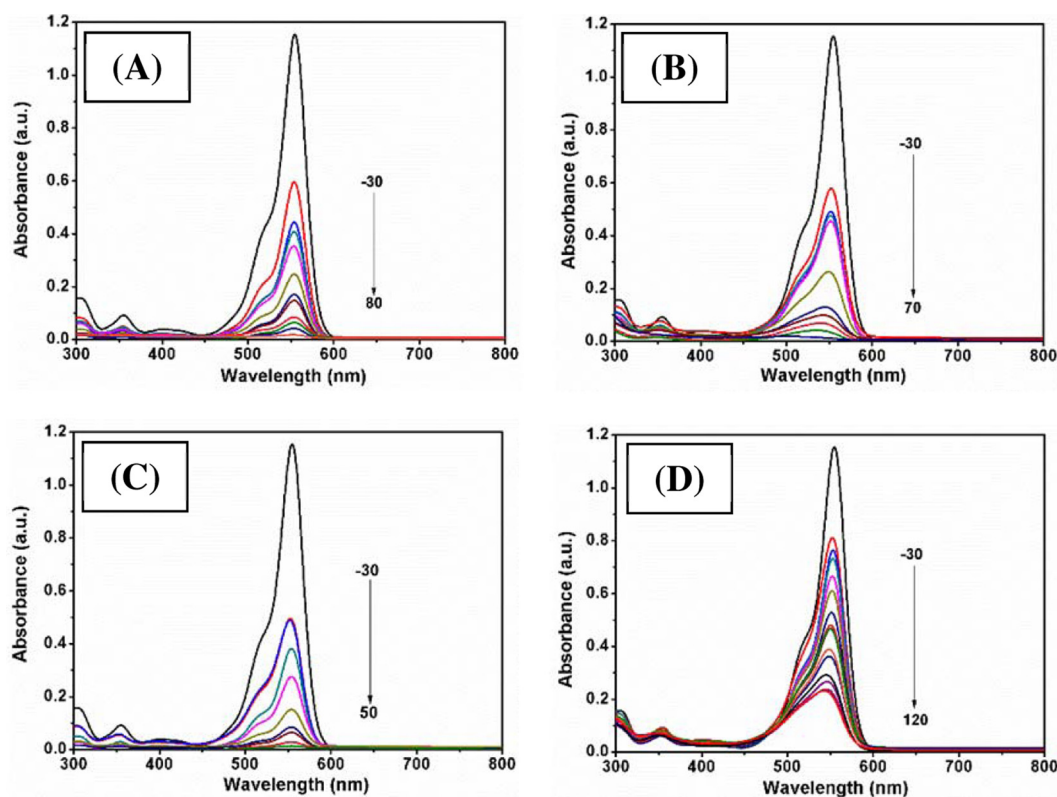
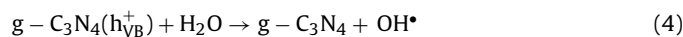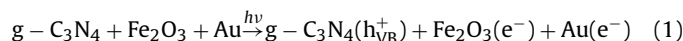Fig. 8. Optical absorbance of RhB solution degraded using different photocatalysts under visible irradiation; (A) Fe_2O_3, (B) g-C_3N_4, (C) Au/g-C_3N_4 (ACN) (D) $FCN_{0.05}$, (E) $FCN_{0.10}$, (F) $FCN_{0.25}$, (G) $FCN_{0.50}$, and (H) $FCN_{1.00}$ hybrid samples.
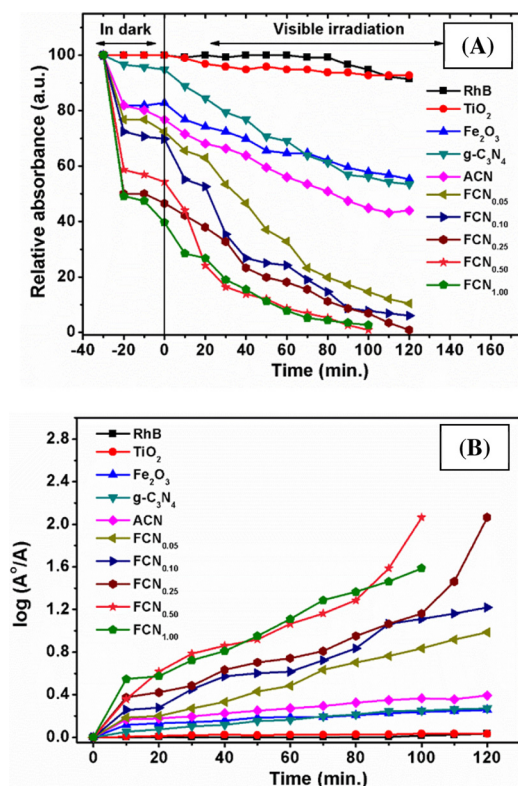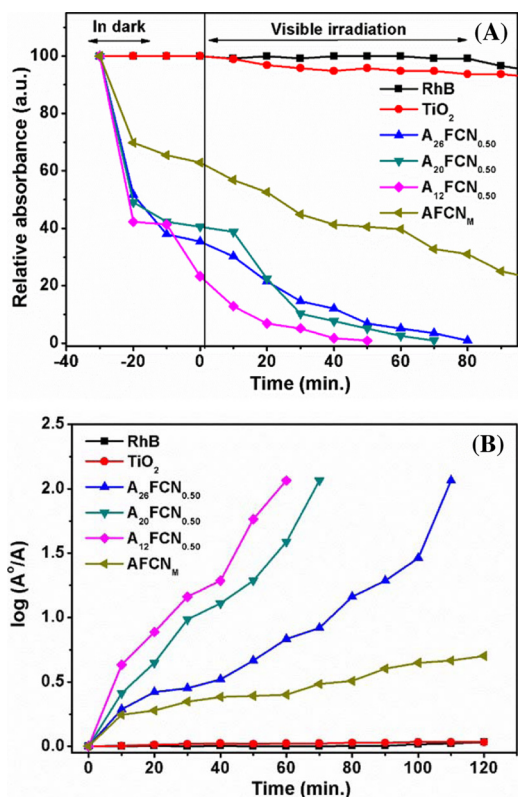
Fig. 9. Photocatalytic activity of Fe_2O_3, g-C_3N_4, ACN, $FCN_{0.05}$, $FCN_{0.10}$, $FCN_{0.25}$, $FCN_{0.50}$, and $FCN_{1.00}$ hybrid photocatalysts for the degradation of rhodamine B (RhB) dye under visible irradiation and (B) ln (A_0/A) versus time curves, where A_0 is the absorbance before irradiation, and $A(t)$ is the absorbance of the dye solution as a function of the irradiation time. Photocatalytic activity of P25 and RhB degradation without the catalyst for comparison.

have a synergetic effect ascribed to the high optical absorbance from SPR induced by Au nanoparticles and the effective separation of photogenerated charge carriers. Additionally, the high electronegativity of the Au nanoparticles could potentially trap photogenerated electrons from the semiconductor, to promote separation of electron–hole pairs.

Based on the results obtained, we propose a possible photocatalysis mechanism for the Au/g-C_3N_4/Fe_2O_3 hybrid photocatalyst. Scheme 1 shows the possible photogeneration and transportation of charge carriers during the photocatalysis process. The energy levels of the semiconductors play a crucial role during photodegradation. The conduction band and valance band energy levels of g-C_3N_4 and Fe_2O_3 are thermodynamically favorable for rapid transportation and separation of charge carriers under visible irradiation [67,68]. As reported in the literature, the CB potential (-3.18 eV versus vacuum) of g-C_3N_4 is more negative than that of Fe_2O_3 (-4.78 eV versus vacuum) [27]. Simultaneously, the work function of an Au nanoparticle is more negative (-5.1 eV versus vacuum), compared with that of the CB levels of g-C_3N_4 and Fe_2O_3 nanostructures, which is more favorable for rapid transportation and separation of photogenerated charge carriers [69]. Possible charge carrier-transfer mechanisms under visible irradiation are given below.

$$g - C_3N_4 + Fe_2O_3 + Au \xrightarrow{h\nu} g - C_3N_4(h_{VB}^+) + Fe_2O_3(e^-) + Au(e^-) \quad (1)$$

$$Au(e^-) + O_2 \rightarrow Au(e^-) \quad (2)$$

$$O_2^- + HO_2^\bullet + H^+ \rightarrow H_2O_2 + O_2 \quad (3)$$

$$g - C_3N_4(h_{VB}^+) + H_2O \rightarrow g - C_3N_4 + OH^\bullet \quad (4)$$

$$H_2O_2 + O_2^- \rightarrow OH + OH^- + O_2 \quad (5)$$

Fig. 10. Optical absorbance of RhB solution degraded using different photocatalysts under visible irradiation; (A) $A_{26}FCN_{0.50}$, (B) $A_{20}FCN_{0.50}$, (C) $A_{12}FCN_{0.50}$, and (D) $AFCN_M$ hybrid samples.

Fig. 11. Photocatalytic activity of $A_{26}FCN_{0.50}$, $A_{20}FCN_{0.50}$, $A_{12}FCN_{0.50}$, and $AFCN_M$ hybrid photocatalysts for the degradation of rhodamine B (RhB) dye under visible irradiation and (B) ln (A_0/A) versus time curves, where A_0 is the absorbance before irradiation, and $A(t)$ is the absorbance of the dye solution as a function of the irradiation time. Photocatalytic activity of P25 and RhB degradation without the catalyst for comparison.
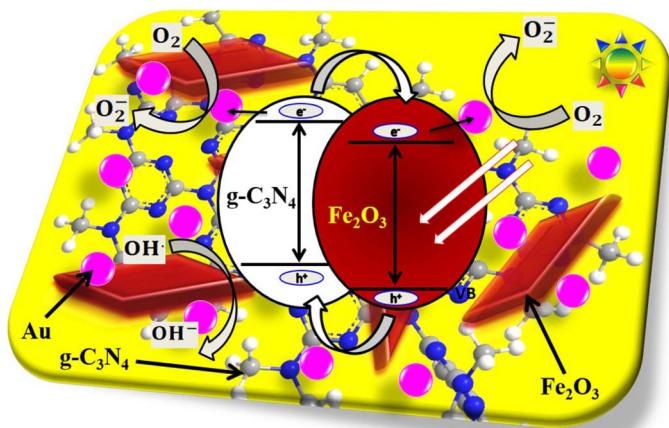

Scheme 1. Photogenerated electrons transportation and degradation of RhB under visible irradiation using $Au/g-C_3N_4/Fe_2O_3$ hybrid sample.

and

$$H_2O_2 + e^-_{CB} \rightarrow OH + OH^-. \tag{6}$$

After visible irradiation, photoelectrons move to the conduction band of the $g-C_3N_4$ as well as Fe_2O_3, leaving behind holes in the valence band. Due to the more negative CB level of $g-C_3N_4$, the photogenerated electrons transfer into the CB of Fe_2O_3 and are then captured immediately by the Au nanoparticles (Eq. (1)). The accumulated photoelectrons captured by the Au nanoparticles take part in the photodegradation process and degrade RhB via reduction (Eqs. (2) and (3)). Simultaneously, the holes in the VB of Fe_2O_3
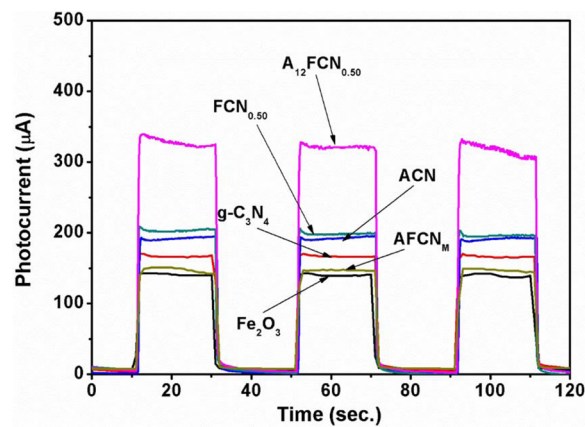
Fig. 12. Transient photocurrent response of Fe_2O_3, $g-C_3N_4$, $FCN_{0.50}$, ACN, $A_{12}FCN_{0.50}$, and $AFCN_M$ hybrid photocatalysts, with on-off cycles of visible irradiation recorded using a Na_2S (0.5 M) electrolyte.

(h^+_{VB}) migrate toward the VB of $g-C_3N_4$ and form highly reactive OH radicals (Eq. (4)), which take part in the degradation of RhB molecules, as given in Eqs. (5) and (6). Therefore, the introduction of Au and $g-C_3N_4$ to the Fe_2O_3 hybrid minimizes the charge carrier recombination rate, resulting in superior photocatalytic activity, compared with that of the bare materials. Additionally, the Au nanoparticles may generate additional charge carriers due to the SPR effect. Thus, the $Au/g-C_3N_4/Fe_2O_3$ hybrid photocatalyst shows superior photocatalytic activity.

3.11. PEC measurements

It is well known that transient photoresponse measurements are the best tools for studying the separation and transportation efficiency of photocatalysts. Hence, we measured the photocurrent generated from the photocatalysts under visible irradiation with several on-off cycles. Fig. 12 shows the photocurrent versus time plot for pure Fe_2O_3 and the hybrid samples. As expected, the Au(12 nm)/$g-C_3N_4/Fe_2O_3$ (323 μA) hybrid generated almost two-fold times higher photocurrent than that of pure Fe_2O_3 (133 μA) and also higher than other samples ($FCN_{0.50}$ = 208 μA, ACN = 190 μA and $AFCN_M$ = 142 μA). This confirms that incorporating Au and $g-C_3N_4$ improved the separation and transportation efficiency of the Fe_2O_3 nanostructure. Moreover, mechanically prepared hybrid sample shows lower photocurrent as compared with that of other hybrids. The higher photocurrent was attributed to SPR and the effective electron transfer between the Fe_2O_3 conduction band and Au nanoparticles. Further, $g-C_3N_4$ sheets covered the absorption below 400 nm, allowing large amounts of visible light photons to generate large numbers of electron–hole pairs resulting in a high photocurrent.

3.12. Open-circuit voltage decay

To examine the effect of Au and $g-C_3N_4$ incorporation on recombination and the kinetics of photocatalysts, we recorded the transient open-circuit voltage (V_{OC}) decay as a function of time under on-off switching of visible irradiation (Fig. 13). The photovoltage decay for the Au(12 nm)/$g-C_3N_4/Fe_2O_3$ hybrid has slower than that of the pure sample, and hybrids fabricated from hydrothermal and mechanically prepared, confirming a longer electron lifetime leading to slower recombination kinetics. The longer lifetime of photoelectrons facilitates the availability of a large number of carriers for photodegradation of organic pollutants. Thus, introducing Au and $g-C_3N_4$ into the Fe_2O_3 nanostructure improved the charge separation efficiency; this contributed to
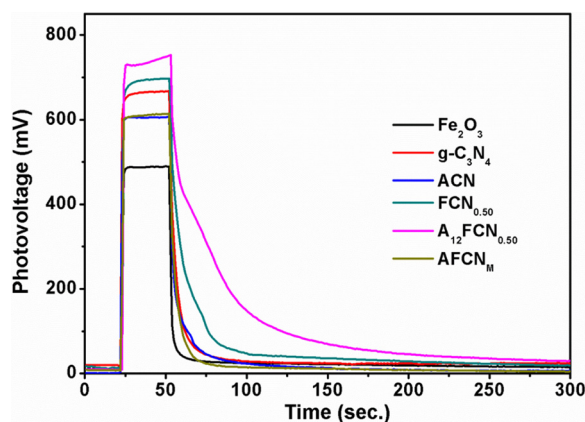
Fig. 13. Open-circuit voltage decay of Fe_2O_3, $g\text{-}C_3N_4$, $FCN_{0.50}$, ACN, $A_{12}FCN_{0.50}$, and $AFCN_M$ hybrid samples, recorded in a Na_2S (0.5 M) electrolyte.
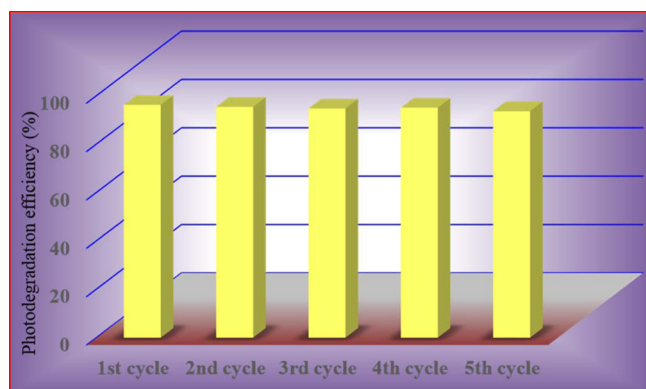

Fig. 14. Reusability of the Au (12 nm)/$g\text{-}C_3N_4$/Fe_2O_3 hybrid photocatalyst toward degradation of RhB under visible irradiation, following five successful experimental runs.

the excellent photocatalytic performance of the $Au/g\text{-}C_3N_4/Fe_2O_3$ hybrid compared with that of the other samples.

3.13. Reusability test

For practical application, it is essential to examine the stability of the photocatalyst. Therefore, we evaluated the stability and reusability of the $Au(12\,nm)/g\text{-}C_3N_4/Fe_2O_3$ hybrid photocatalyst by repeating the photodegradation experiment for five cycles under same conditions. Fig. 14 illustrates the degradation of RhB over five cycles carried out under visible irradiation. No obvious change was evident in the photodegradation efficiency. These results confirmed that the $Au/g\text{-}C_3N_4/Fe_2O_3$ hybrid photocatalyst was stable, verifying its usability for water purification and splitting applications.

4. Conclusions

In summary, we explored efficient, reusable visible light using an $Au/g\text{-}C_3N_4/Fe_2O_3$ hybrid photocatalyst synthesized by simple, cost-effective processes at room temperature. Structural, surface, optical, and elemental analysis confirmed strong interactions and heterojunction formation among the Au, $g\text{-}C_3N_4$, and Fe_2O_3 phases in the hybrid sample. Compared with pristine Fe_2O_3 and $g\text{-}C_3N_4$ samples, the $Au/g\text{-}C_3N_4/Fe_2O_3$ hybrid exhibited almost 16-fold higher kinetic rate constant for RhB degradation under visible irradiation. The superior photocatalytic performance of the hybrid photocatalyst was attributed to (i) the high surface area for dye adsorption, (ii) the high optical absorbance for charge carrier generation, (iii) the capture of electrons by conductive Au particles

leading to rapid separation, and (iv) the SPR of Au nanoparticles allowing the generation of a large number of carriers under visible irradiation. Compared with hematite and other hybrids, $Au/g\text{-}C_3N_4/Fe_2O_3$ hybrid showed highest photocurrent, confirming the effective transportation of charge carriers. Further, open-circuit voltage decay measurements indicated a longer lifetime for the carriers in the $Au/g\text{-}C_3N_4/Fe_2O_3$ hybrid photocatalyst. A possible photocatalysis mechanism was proposed based on the results. From the measured photocatalytic activity and analysis, Au and $g\text{-}C_3N_4$ incorporation into the rhombohedral structure of Fe_2O_3 has a synergetic effect and reduces the recombination losses in pristine material. Thus, the $Au/g\text{-}C_3N_4/Fe_2O_3$ hybrid photocatalyst is a promising photocatalytic material for the utilization of solar energy and the development of an efficient device for remediation of environmental pollutants.

Appendix A. Supplementary data

Supplementary data associated with this article can be found, in the online version, at http://dx.doi.org/10.1016/j.apcatb.2015.04.045.

References

[1] M.N. Chong, B. Jin, C.K. Chow, C. Saint, Water Res. 44 (2010) 2997–3027.
[2] K. Hashimoto, H. Irie, A. Fujishima, Jpn. J. Appl. Phys. 44 (2005) 8269–8285.
[3] G. Palmisano, V. Augugliaro, M. Pagliaro, L. Palmisano, Chem. Commun. 33 (2007) 3425–3437.
[4] A. Fujishima, K. Honda, Nature 238 (1972) 37–38.
[5] D. Bahnemann, Sol. Energy 77 (2004) 445–459.
[6] Y. Niu, M. Xing, B. Tian, J. Zhang, Appl. Catal. B: Environ. 115–116 (2012) 253–260.
[7] W. Fang, M. Xing, J. Zhang, Appl. Catal. B: Environ. 160–161 (2014) 240–246.
[8] Z. Zou, J. Ye, K. Sayama, H. Arakawa, Nature 414 (2001) 625–627.
[9] R. Yerga, M. Galvn, F. Valle, J. Mano, J. Fierro, ChemSusChem 2 (2009) 471–485.
[10] H. Kisch, Angew. Chem. Int. Ed. 52 (2013) 812–847.
[11] D.K. Bora, A. Braun, E.C. Constable, Energy Environ. Sci. 6 (2013) 407–425.
[12] Z.G. Zhao, M. Miyauchi, Angew. Chem. Int. Ed. 47 (2008) 7051–7055.
[13] J. Li, J. Yan, C. Liu, L. Dong, H. Lv, W. Sun, S. Xing, CrystEngComm 16 (2014) 10943–10948.
[14] S. Linic, P. Christopher, D.B. Ingram, Nat. Mater. 10 (2011) 911–921.
[15] W. Hou, S.B. Cronin, Adv. Funct. Mater. 23 (2013) 1612–1619.
[16] B. Qiu, M. Xing, J. Zhang, J. Am. Chem. Soc. 136 (2014) 5852–5855.
[17] S.C. Warren, K. Voitchovsky, H. Dotan, C.M. Leroy, M. Cornuz, F. Stellacci, C. Hebert, A. Rothschild, M. Gratzel, Nat. Mater. 12 (2013) 842–849.
[18] D.A. Wheeler, G. Wang, Y. Ling, Y. Li, J.Z. Zhang, Energy Environ. Sci. 5 (2012) 6682–6702.
[19] S.K. Mohapatra, S.E. John, S. Banerjee, M. Misra, Chem. Mater. 21 (2009) 3048–3055.
[20] W. Zhou, L. Lin, W. Wang, L. Zhang, Q. Wu, J. Li, L. Guo, J. Phys. Chem. C 115 (2011) 7126–7133.
[21] K. Sivula, R. Zboril, F.L. Formal, R. Robert, A. Weidenkaff, J. Tucek, J. Frydrych, M. Gratzel, J. Am. Chem. Soc. 132 (2010) 7436–7444.
[22] S. Chaudhari, D. Bhattacharjya, J.S. Yu, RSC Adv. 3 (2013) 25120–25128.
[23] D. Wang, D. Astruc, Chem. Rev. 114 (2014) 6949–6985.
[24] K. Sivula, F.L. Formal, M. Gratzel, ChemSusChem 4 (2011) 432–449.
[25] X. Wang, S. Blechert, M. Antonietti, ACS Catal. 2 (2012) 1596–1606.
[26] X. Wang, K. Maeda, A. Thomas, K. Takanabe, G. Xin, J.M. Carlsson, K. Domen, M. Antonietti, Nat. Mater. 8 (2009) 76–80.
[27] D.S. Su, J. Zhang, B. Frank, A. Thomas, X. Wang, J. Paraknowitsch, R. Schlcgl, ChemSusChem 3 (2010) 169–180.
[28] S. Ye, L.G. Qiu, Y.P. Yuan, Y.J. Zhu, J. Xia, J.F. Zhu, J. Mater. Chem. A 1 (2013) 3008–3015.
[29] Y. Liu, Y.X. Yu, W.D. Zhang, Int. J. Hydrogen Energy 39 (2014) 9105–9113.

[30] J. Theerthagiri, R.A. Senthil, A. Priya, J. Madhavan, R.J.V. Michael, M. Ashokkumar, RSC Adv. 4 (2014) 38222–38229.
[31] C. Wang, D. Astruc, Chem. Soc. Rev. 43 (2014) 7188–7216.
[32] I. Thomann, B.A. Pinaud, Z. Chen, B.M. Clemens, T.F. Jarmillo, M.L. Brongersma, Nano Lett. 11 (2011) 3440–3446.
[33] L. Gomez, V. Sebastian, M. Arruebo, J. Santamaria, S.B. Cronin, Phys. Chem. Chem. Phys. 16 (2014) 15111–15116.
[34] R.C. Pawar, D. Choi, C.S. Lee, Int. J. Hydrogen Energy 40 (2014) 1–12.
[35] J. Kimling, M. Maier, B. Okenve, V. Kotaidis, H. Ballot, A. Plech, J. Phys. Chem. B 110 (2006) 15700–15707.
[36] J. Liu, T. Zhang, Z. Wang, G. Dawson, W. Chen, J. Mater. Chem. 21 (2011) 14398–14401.
[37] Y. Zhang, T. Mori, L. Niu, J. Ye, Energy Environ. Sci. 4 (2011) 4517–4521.
[38] H. Singh, S. Bhagwat, S. Jouen, B. Lefez, A.A. Athawale, B. Hannoyer, S. Ogale, Phys. Chem. Chem. Phys. 12 (2010) 3246–3253.
[39] J. Stajdohar, M. Ristic, S. Music, J. Mol. Struct. 1044 (2013) 290–298.
[40] X. Gou, G. Wang, X. Kong, D. Wexler, J. Horvat, J. Yang, J. Park, Chem. Eur. J. 14 (2008) 5996–6002.
[41] K. Woo, H.J. Lee, J.P. Ahn, Y.S. Park, Adv. Mater. 15 (2003) 1761–1764.
[42] D. Chen, W. Wei, R. Wang, J. Zhu, L. Guo, New J. Chem. 36 (2012) 1589–1595.
[43] H. Ji, F. Chang, X. Hu, W. Qin, J. Shen, Chem. Eng. J. 218 (2013) 183–190.
[44] J. Zhang, F. Guo, X. Wang, Adv. Funct. Mater. 23 (2013) 3008–3014.
[45] M.J. Bojdys, J.O. Muller, M. Antonietti, A. Thomas, Chem. Eur. J. 14 (2008) 8177–8182.
[46] S. Yang, C. Wang, L. Ma, Y. Peng, Z. Qu, N. Yan, J. Chen, H. Chang, J. Li, Catal. Sci. Technol. 3 (2013) 161–168.
[47] K. Song, Y. Lee, M.R. Jo, K.M. Nam, Y.M. Kang, Nanotechnology 23 (2012) 505101–505106.
[48] F.L. Souza, K.P. Lopes, P. Nascente, E.R. Leite, Sol. Energy Mater. Sol. Cells 93 (2009) 362–368.
[49] G.K. Pradhan, K.M. Parida, ACS Appl. Mater. Interfaces 3 (2011) 317–323.
[50] S. Yang, Y. Guo, N. Yan, D. Wu, H. He, Z. Qu, J. Jia, Ind. Eng. Chem. Res. 50 (2011) 9650–9656.
[51] S. Yang, Y. Guo, N. Yan, Z. Qu, J. Xie, C. Yang, J. Jia, J. Hazard. Mater. 186 (2011) 508–515.
[52] A.P. Grosvenor, B.A. Kobe, M.C. Biesinger, N.S. Mclntyre, Surf. Interface Anal. 36 (2004) 1564–1574.
[53] G. Dong, L. Zhang, J. Mater. Chem. 22 (2012) 1160–1166.
[54] D. Gao, Q. Xu, J. Zhang, Z. Yang, M. Si, Z. Yan, D. Xue, Nanoscale 6 (2014) 2577–2581.
[55] H. Dai, X. Gao, E. Liu, Y. Yang, W.Q. Hou, L.M. Kang, J. Fan, X. Hu, Diamond Relat. Mater. 38 (2013) 109–117.
[56] M.P. Casaletto, A. Longo, A. Martorana, A. Prestianni, A.M. Venezia, Surf. Interface Anal. 38 (2006) 215–218.
[57] S. Yang, Y. Gong, J. Zhang, L. Zhan, L. Ma, Z. Fang, R. Vajtai, X. Wang, P.M. Ajayan, Adv. Mater. 25 (2013) 2452–2456.
[58] J.P. Sylvestre, S. Poulin, A.V. Kabashin, E. Sacher, M. Meunier, J.H. Luong, J. Phys. Chem. B 108 (2004) 16864–16869.
[59] A.M. Visco, F. Neri, G. Neri, A. Donato, C. Milone, S. Galvagno, Phys. Chem. Chem. Phys. 1 (1999) 2869–2873.
[60] E. Thimsen, F.L. Formal, M. Gratzel, S.C. Warren, Nano Lett. 11 (2011) 35–43.
[61] J. Zhang, X. Liu, L. Wang, T. Yang, X. Guo, S. Wu, S. Wang, S. Zhang, J. Phys. Chem. C 115 (2011) 5352–5357.
[62] F. Ji, C. Li, X. Wei, J. Yu, Chem. Eng. J. 231 (2012) 434–440.
[63] Y. Xia, L. Yin, Phys. Chem. Chem. Phys. 15 (2013) 18627–18634.
[64] I.K. Konstantinou, T.A. Albanis, Appl. Catal. B: Environ. 49 (2004) 1–14.
[65] M. Murdoch, G.I.N. Waterhouse, M.A. Nadeem, J.B. Metson, M.A. Keane, R.F. Howe1, J. Llorca, H. Idriss, Nat. Chem. 3 (2011) 489–492.
[66] V. Subramanian, E.E. Wolf, P.V. Kamat, J. Am. Chem. Soc. 126 (2004) 4943–4950.
[67] B. Chai, T. Peng, J. Mao, K. Li, L. Zan, Phys. Chem. Chem. Phys. 14 (2012) 16745–16752.
[68] S. Zhang, F. Ren, W. Wu, J. Zhou, L. Sun, X. Xiao, C. Jiang, J. Colloid Interface Sci. 427 (2014) 29–34.
[69] S.C. Warrne, E. Thimsen, Energy Environ. Sci. 5 (2012) 5133–5146.